ACS APPLIED MATERIALS & INTERFACES

www.acsami.org

Research Article

Effects of Anisotropic Strain on Spin−Orbit Torque Produced by the Dirac Nodal Line Semimetal IrO_2

Arnab Bose,* Jocienne N. Nelson, Xiyue S. Zhang, Priyamvada Jadaun, Rakshit Jain, Darrell. G. Schlom, Daniel. C. Ralph, David. A. Muller, Kyle. M. Shen, and Robert. A. Buhrman

Cite This: *ACS Appl. Mater. Interfaces* 2020, 12, 55411−55416

Read Online

ACCESS | Metrics & More | Article Recommendations | Supporting Information

ABSTRACT: We report spin-torque ferromagnetic resonance studies of the efficiency of the damping-like (ξ_{DL}) spin−orbit torque exerted on an adjacent ferromagnet film by current flowing in epitaxial (001) and (110) IrO_2 thin films. IrO_2 possesses Dirac nodal lines (DNLs) in the band structure that are gapped by spin−orbit coupling, which could enable a very high spin Hall conductivity, σ_{SH}. We find that the (001) films do exhibit exceptionally high ξ_{DL} ranging from 0.45 at 293 K to 0.65 at 30 K, which sets the lower bounds of σ_{SH} to be 1.9×10^5 and 3.75×10^5 Ω^{-1} m^{-1}, respectively, 10 times higher and of opposite sign than the theoretical prediction. Furthermore, ξ_{DL} and σ_{SH} are substantially reduced in anisotropically strained (110) films. We suggest that this high sensitivity to anisotropic strain is because of changes in contributions to σ_{SH} near the DNLs.

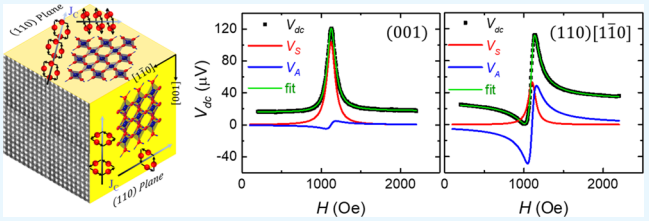

KEYWORDS: *complex oxide heterostructures, spin−orbit-torques, Dirac nodal line (DNL), crystal symmetry, strain and band topology, anisotropic spin Hall conductivity, spin-torque ferromagnetic resonance (ST-FMR)*

1. INTRODUCTION

Since the discovery of a "giant" spin Hall effect (SHE)[1] in certain heavy metal elements there has been an intense effort to identify and develop new and technologically viable, heavy metal-based thin film materials that could generate spin currents with even greater efficiency to exert spin−orbit torques (SOTs)[2] on adjacent ferromagnetic nanostructures. In parallel, there have been wide ranging fundamental studies of the spin currents that can arise from robust, intrinsic spin−orbit coupling (SOC) effects in more exotic systems, including topological insulators,[3,4] transition-metal dichalcogenides with a broken crystalline symmetry,[5] and Weyl[6] and Dirac semimetals,[7] where gap-less electronic excitations are protected by topology and symmetry. Here, we experimentally study strong SOT from the topological Dirac nodal line semimetal IrO_2 in (001) and (110) normal films, which we find to exhibit distinctly different values of spin Hall conductivity.

A recent focus of SOT research has been the semimetal $SrIrO_3$, where theoretical calculations and angle-resolved photoemission spectroscopy (ARPES) indicate that the tilt of the IrO_6 octahedra in the orthorhombic phase leads to narrow t_{2g} conduction bands with near-degeneracies and band crossings protected by the nonsymmorphic crystal symmetry.[8−10] SOT measurements on $SrIrO_3$/ferromagnet (FM) bilayers show a large effective-spin Hall conductivity (SHC) $\sigma_{SH}^{eff} \sim 10^5$ Ω^{-1} m^{-1}.[11−14] Here, $\sigma_{SH}^{eff} \equiv T_{int}\sigma_{SH}$, where $T_{int}(<1)$ is the interfacial spin transparency and σ_{SH} is the actual SHC of the material. It is intriguing that refs 11 and 12 report opposite signs of ξ_{DL} and also that a significant in-plane crystalline anisotropy is reported for ξ_{DL} in refs 11 and 13 but not in ref 12. The simplest iridate is IrO_2, which in the rutile phase consists of chains of edge-sharing IrO_6 octahedra running along the *c*-axis with corner-sharing connections among counter-rotated neighboring chains in the (001) plane. Because of the mixture of both edge- and corner-sharing IrO_6 octahedra, and a relatively direct coordination between Ir atoms that provides an additional hopping channel, the overall result is increased p−d orbital hybridization, which broadens the t_{2g} conduction band compared to other, corner-sharing, iridates.[8−10] This reduced electron correlation, which also is found in tetragonal $SrIrO_3$ where neighboring octahedra are not counter-rotated thereby resulting in larger bandwidths, might suggest that IrO_2 would be a material with a relatively low SHC, as is reported for tetragonal $SrIrO_3$.[11] Recent ab initio density functional theory (DFT) calculations, however, indicate that the IrO_2 band structure contains two types of Dirac nodal lines (DNLs) associated with the crystal symmetries of the rutile structure.[15] Type-1 DNLs allow an anticrossing near the Fermi surface because of SOC and can therefore contribute a large SHC with a predicted maximum value of $-2.5 \times 10^4(\hbar/2e)$ Ω^{-1} m^{-1},[15,16] roughly in accord

Received: September 12, 2020
Accepted: November 12, 2020
Published: November 24, 2020

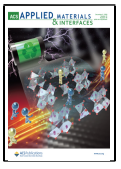

https://dx.doi.org/10.1021/acsami.0c16485
ACS Appl. Mater. Interfaces 2020, 12, 55411−55416

with the results of an early inverse-SHE study of polycrystalline/amorphous IrO_2 films, although of an opposite sign.[17] Subsequent ARPES studies confirmed the existence of DNLs in epitaxial IrO_2 thin films and bulk crystals.[18,19] (See the Supporting Information for a more-detailed description of the two types of DNLs.)

Here, we report values of σ_{SH}^{eff} for (001) and (110) IrO_2 films grown epitaxially on TiO_2 rutile substrates as determined by spin-torque ferromagnetic resonance (ST-FMR) measurements of the efficiency of the damping-like ξ_{DL} and field-like ξ_{FL} spin torques, exerted on an adjacent $Ni_{80}Fe_{20}$ (Py) thin film. σ_{SH}^{eff} is then obtained from $\sigma_{SH}^{eff} = \xi_{DL}\sigma_e$, where σ_e is the film's electrical conductivity. Because of the thermodynamically favored reactions between Fe and IrO_2[20] and the unavoidable presence of undercoordinated O ions at the surfaces of a rutile film,[21] the Fe in the Py near the interface becomes oxidized if deposited directly on IrO_2. We therefore inserted a thin Ir passivation layer (~1 nm) between the IrO_2 and the Py to avoid this oxidation (Figure 1d–g). (We have determined that Ir has a minimal SHE, $\xi_{DL} \leq 0.02$). Even with the significant spin-current attenuation arising from this Ir layer, at room temperature (RT), we measured ξ_{DL} to be 0.45

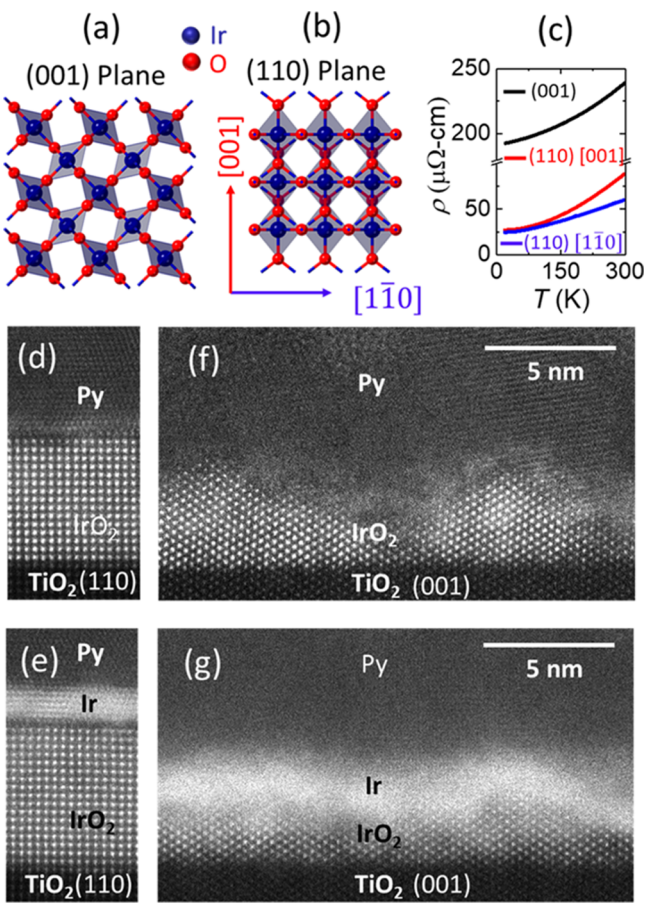

Figure 1. (a,b) Schematic top-down view representation of the (001) and (110) plane of IrO_2 illustrating the edge to corner connectivity of the octahedra in the (001) plane as opposed to the corner to corner and edge to edge connectivity in the (110) plane. (c) Resistivity of (001) and (110) IrO_2 films as a function of temperature and for the two different principal axes [1$\bar{1}$0] and [001] of the (110) film. (d–g) Annular dark-field STEM image of (110) IrO_2/Py, (110) IrO_2/Ir/Py, (001) IrO_2/Py, and (001) IrO_2/Ir/Py, respectively.

for current flow in the plane of the low σ_e (001) films, rising to 0.65 at 30 K, corresponding to $\sigma_{SH}^{eff} = 1.9 \times 10^5(\hbar/2e)\ \Omega^{-1}\ m^{-1}$ at RT and $3.75 \times 10^5(\hbar/2e)\ \Omega^{-1}\ m^{-1}$ at 30 K. These lower bounds are more than an order of magnitude higher, and of opposite sign, than the available theoretical predictions for σ_{SH}.[15,16] For the (110) IrO_2 films, which are anisotropically strained, the SHC is substantially reduced even though σ_e is increased (Figure 1c), and both quantities are slightly anisotropic. At RT in the (110) films, σ_{SH}^{eff} varies from $7.8 \times 10^4(\hbar/2e)$ to $8.8 \times 10^4(\hbar/2e)\ \Omega^{-1}\ m^{-1}$ for the current applied along the lower conductivity [001] and higher conductivity [1$\bar{1}$0] directions. The anisotropy in σ_{SH}^{eff} increases as σ_e increases with decreasing temperature (T), with σ_{SH}^{eff} becoming 9.6×10^4 and $1.85 \times 10^5\ \Omega^{-1}\ m^{-1}$, respectively, at 30 K. We attribute the large reduction of σ_{SH}^{eff} in the anisotropically strained (110) IrO_2 compared to isotropically strained (100) IrO_2 as being because of high sensitivity to the strain for the contributions to σ_{SH}^{eff} near the DNLs.

2. EXPERIMENTS AND RESULTS

2.1. Sample Characterization. For this study, we grew IrO_2 thin films of 5 nm thickness by reactive oxide molecular beam epitaxy on (001) and (110) single-crystal TiO_2 substrates at 300 C, as described in Supporting Information[22] and in refs 9 and 10. On (001) TiO_2, IrO_2 grows centrosymmetrically with a coherent, isotropic in-plane biaxial tensile strain of $\epsilon_{11} = \epsilon_{22} \approx 2\%$. The nonsymmorphic symmetries of IrO_2 are preserved under this isotropic strain. In contrast, the (110) films grow with a compressive strain (~−5%) in the [001] direction and a tensile strain (~2%) in the [1$\bar{1}$0] direction films because of the lattice mismatch between IrO_2 and (110) TiO_2. It has been found that this anisotropic strain for (110) IrO_2 films persists up to at least a 16 nm thickness.[10] This strain breaks the nonsymmorphic symmetries of the (110) films.

The T-dependent resistivities of the different films and for different current directions in the (110) case are shown in Figure 1c. The resistivity of the (001) film, which is independent of the direction of current flow, is high and exhibits only a small residual resistivity ratio (RRR). The (110) films have lower resistivity and higher RRR, indicative of a cleaner metal, with the resistivity being dependent upon the direction of the current flow. This anisotropy does not, however, appear to be due primarily to the anisotropic strain in these films because the nearly 50% difference in resistivity at RT between the current flow in the [001] and [1$\bar{1}$0] directions, as shown in Figure 1c, is roughly consistent with the 77% difference in resistivity at RT in unstrained IrO_2 single crystals.[23−25]

For the ST-FMR measurements,[26−28] four series of multilayers were prepared as described in ref 22. Series 1: (001)IrO_2(5 nm)/Ir(1 nm)/Py(3−6 nm)/TaO_x(1.5 nm); series 2: (110)IrO_2(5 nm)/Ir(1 nm)/Py(3−6 nm)/TaO_x(1.5 nm); series 3: (001)IrO_2(5 nm)/Py(3−7 nm)/TaO_x(l.5 nm); and series 4: (110)IrO_2(5 nm)/Py(2.7−7 nm)/TaO_x(1.5 nm). The multilayers with the Ir passivation layer, series 1 and 2, were the major focus of the SOT study, while series 3 and 4 were used to quantify the benefit and cost of the use of the Ir spacer.

Cross sections of examples of each of the four types of the IrO_2 multilayer were examined by high-resolution scanning transmission electron microscopy (STEM) and electron energy loss spectroscopy (EELS). Annular dark-field STEM

https://dx.doi.org/10.1021/acsami.0c16485
ACS Appl. Mater. Interfaces 2020, 12, 55411−55416

images of the cross sections are shown in Figure 1d–g. The epitaxial (110) films are atomically flat on the lateral scale of the cross-sectional image, while the Py is polycrystalline, both with and without the textured Ir spacer (Figure 1d,e). The (001) IrO_2 films are faceted and rough (Figure 1f,g), which is consistent with the high surface energy of the (001) rutile surface.[29] The faceted IrO_2 (001) surface is most clearly seen in the sample without the Ir spacer (Figure 1f) as the latter wets the surfaces of the IrO_2 facets, obscuring the dark-field contrast with the Py. Spatially resolved EELS measurements show that Ir is quite effective in passivating the surface of IrO_2 for both the (110) and the faceted (001) films, with there being no signal of the oxidized Fe atoms.[22] For the samples without the Ir spacer, the EELS data indicate significant Fe-oxidation in the vicinity of the IrO_2 surface for the faceted (001) films. There is less Fe oxide at the unpassivated (110) IrO_2 surface, consistent with the lower density of under coordinated O ions at the (110) rutile surface.

2.2. SOT Results. The details of the ST-FMR technique we used are provided in ref 22. In brief, we measure the FMR resonant response to a microwave current applied to the HM/FM coplanar waveguide in the presence of an in-plane magnetic field. This response consists of a symmetric Lorentzian voltage signal of amplitude S centered about the resonant field H_o because of the in-plane damping-like torque, and an antisymmetric Lorentzian response, of amplitude A, to the out-of-plane torque resulting from the microwave Oersted field generated by the current flowing in the HM, plus any additional interfacial field-like torque contribution from the incident spin current. The result can be expressed in terms of a quantity ξ_{FMR}[27] where

$$\frac{1}{\xi_{FMR}} \equiv \frac{A}{S}\left(\frac{\hbar}{e}\right)\Big/\left(\mu_0 M_s d_{Py} d_{IrO_2}\sqrt{1+\left(\frac{M_{eff}}{H_0}\right)}\right) = \frac{1}{\xi_{DL}}\left(1+\frac{\hbar}{e}\frac{\xi_{FL}}{\mu_0 M_s d_{Py} d_{IrO_2}}\right) \quad (1)$$

here d_{Py} and d_{IrO_2} are the thicknesses of the Py and IrO_2 layers, M_s is the saturation magnetization of the Py as measured by vibrating sample magnetometry, and M_{eff} is the Py's out-of-plane demagnetization field.

In Figure 2, we show plots of $1/\xi_{FMR}$ versus $1/d_{Py}$ as obtained at RT for all four series of samples. The $1/d_{Py} = 0$ intercepts of the linear fits to the variation of $1/\xi_{FMR}$ provide $1/\xi_{DL}$, while ξ_{FL} is determined from the slope of the linear fit to eq 1. The results are presented in Table 1. The high-resistivity (001) IrO_2 with the 1 nm passivation layer exhibits an exceptionally high, $\xi_{DL} = 0.45 \pm 0.03$ (Figure 2a), notwithstanding the spin-current attenuation of the Ir spacer. The lower resistivity (110) films with the Ir spacer have lower ξ_{DL} along the $[1\bar{1}0]$ and (001) directions with a smaller anisotropy in σ_{SH}^{eff}, as shown in Table 1.

When the Ir spacer layer was not utilized for the (001) IrO_2 films, the result was more than a factor of three degradations of ξ_{DL} from the Ir-passivated result (Figure 2c,d), which we attribute to the substantial oxidation of the interfacial iron in the Py layer, as revealed by the EELS study.[22] In contrast, in the absence of the Ir spacer for the (110) samples, ξ_{DL} is approximately doubled in amplitude for both the $[1\bar{1}0]$ and [001] directions, and with a sign reversal of ξ_{FL}. We conclude that the degree of interfacial Fe-oxidation indicated by EELS

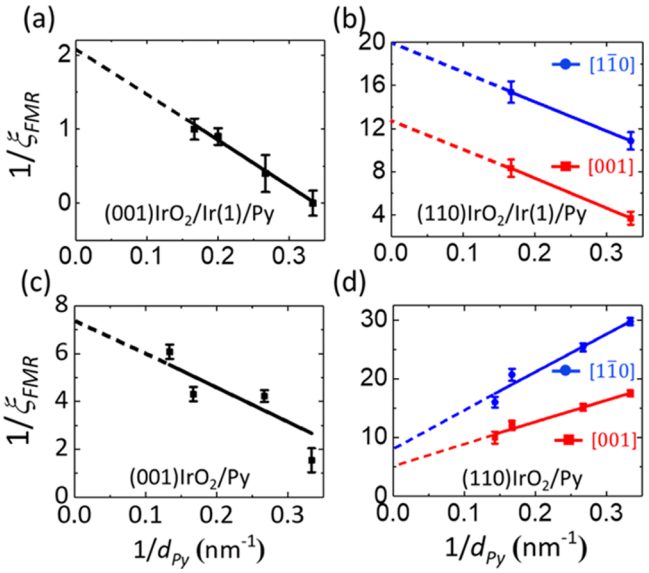

Figure 2. Inverse of the ST-FMR apparent spin-torque efficiency ($1/\xi_{FMR}$) at RT as a function of the inverse of Py thickness ($1/d_{Py}$) for the different series of samples: (a) (001)IrO_2/Ir(1)/Py; (b) (110)IrO_2/Ir(1)/Py for both the $[1\bar{1}0]$ (red color) and [001] directions (black color); (c) (001)IrO_2/Py; and (d) (110)IrO_2/Py.

for the atomically smooth (110) films is not very detrimental, if at all, to interfacial spin transport. From the (110) results, we estimate the Ir spin-diffusion length λ_s to be ~1.2 nm, which is consistent with a recent work.[30] This results in the attenuation of the spin current entering the Ir layer from the IrO_2 by approximately 50% before it impinges on the Py.

2.3. Temperature Dependence of SOT. We measured the SOTs of the Ir-passivated samples from RT to 30 K, with the results shown in Figure 3. For the high-resistivity (001), IrO_2 films both ξ_{DL} and ξ_{FL} increased substantially as T was decreased, with ξ_{DL} reaching 0.65 ± 0.07 at 30 K and with the proportionate increase in ξ_{FL} being even larger (Figure 3a). For current flow in both the $[1\bar{1}0]$ and [001] directions of the (110) films, ξ_{DL} decreased with decreasing T, with the percentage decrease being larger for the lower resistivity $[1\bar{1}0]$ direction. The field-like torque efficiency ξ_{FL} was smaller than ξ_{DL}, and increased with decreasing T for the $[1\bar{1}0]$ direction (Figure 3b) and was more or less constant for the higher resistivity [001] direction (Figure 3c). The quite variable behavior of ξ_{FL} is suggestive that the role of the interface is more complex than, for example, is the case for typical Pt/FM systems.

3. DISCUSSION

We have used the results presented in Figure 3a–c along with the measured variation of the resistivity (Figure 1c) to obtain the variation of σ_{SH}^{eff} for the two different Ir-passivated IrO_2 surfaces and for the two principal directions of the (110) samples, both as a function of T and σ_e. The results are shown in Figure 3d,e. The T-dependent resistivity indicates that IrO_2 has a metallic behavior (Figure 1c) with electron transport through the t_{2g} conduction band. For the intrinsic SHE, it is expected that σ_{SH} should be more or less independent of σ_e in the "clean metal" regime where carrier lifetime is not a factor in determining the overall spin Berry curvature and hence σ_{SH}.[31] However, as σ_e decreases, that is as the carrier lifetime becomes shorter, σ_{SH} is expected to degrade, at first gradually and then

https://dx.doi.org/10.1021/acsami.0c16485
ACS Appl. Mater. Interfaces 2020, 12, 55411–55416

Table 1. Values for the Damping-like and Field-like Spin-Torque Efficiencies, as Measured at RT by ST-FMR, for 5 nm Epitaxial IrO_2 Films with and without a 1 nm Ir Passivation Layer between the IrO_2 and the Py Spin-Current Detector Layer

parameters	(001)/Ir/Py	(001)/Py	(110)[1$\bar{1}$0]/Ir/Py	(110)[1$\bar{1}$0]/Py	(110)[001]/Ir/Py	(110)[001]/Py
ξ_{DL}	0.45 ± 0.03	0.14 ± 0.01	0.05 ± 0.008	0.12 ± 0.01	0.08 ± 0.01	0.18 ± 0.01
ξ_{FL}	−0.05 ± 0.005	−0.01 ± 0.005	−0.02 ± 0.005	0.04 ± 0.005	−0.02 ± 0.005	0.02 ± 0.005
σ_{SHE}^{eff} ($10^5\hbar/2e\ \Omega^{-1}\ m^{-1}$)	1.9 ± 0.15	0.57 ± 0.05	0.78 ± 0.11	1.95 ± 0.2	0.88 ± 0.12	2.13 ± 0.2

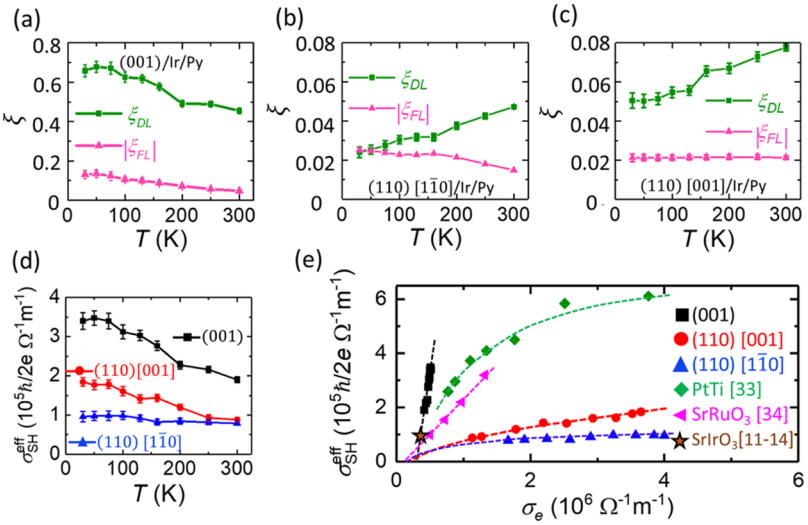

Figure 3. Temperature dependence of ξ_{DL} and $|\xi_{FL}|$ of the Irpassivated samples for the (001) IrO_2/Ir(1)/Py series (a), (110) IrO_2/Ir(1)/Py series in the low-resistivity [1$\bar{1}$0] direction (b), and (110) series along high-resistive [001] direction (c). (d) σ_{SH}^{eff} as a function of temperature for three different cases. (e) σ_{SH}^{eff} as a function of electrical conductivity (σ_e) of the 5 nm IrO_2 films for the three different cases. Also shown for qualitative comparison are published results of σ_{SH}^{eff} vs σ_e for $SrRuO_3$, $SrIrO_3$, and 6 nm Pt films where variable numbers of sub-monolayer insertions of Ti were employed to vary σ_e.

more rapidly as σ_e decreases further into a "dirty metal" regime.[31] Previous studies have examined the transition between the dirty and clean metal regimes of the SHE in Pt-based alloys and composites[32,33] and epitaxial $SrRuO_3$ thin films,[34] which we compare with the IrO_2 films by plotting σ_{SH}^{eff} versus σ_e, as shown in Figure 3e. (We point out that these plots are only qualitative comparisons that do not account for the differences in carrier density and band structure between the different materials.)

The nearly constant σ_{SH}^{eff} with varying σ_e (temperature) for the (110) IrO_2 film with current flow in the low-resistivity [1$\bar{1}$0] direction suggests that in this case the material is in or near the clean metal regime, while the behavior for current in the [001] direction shows only a somewhat greater variation with σ_e and a slightly larger amplitude overall (Figure 3e). For the (001) film in contrast, σ_{SH}^{eff} decreases strongly with decreasing σ_e, which is a signature of the dirty metal regime, but nevertheless σ_{SH}^{eff} still exhibits a quite high maximum value, $3.75 \times 10^5(\hbar/2e)\ \Omega^{-1}\ m^{-1}$ (Figure 3e). The approximately linear variation of σ_{SH}^{eff} with σ_e suggests that σ_{SH}^{eff} would further increase and saturate at an even higher value than that measured here if a sufficiently higher quality, lower defect density (001) film could be produced with a high enough σ_e to be near or in the clean metal regime. We also note that because the variations in σ_{SH}^{eff} between the different types of epitaxial IrO_2 films and the different current directions of the (110) films do not fall along a common scaling curve as a function of σ_e ($\sigma_{SH}^{eff} = \theta_{SH}\sigma_e$), it appears that the primary cause of the difference is not simply due to the difference in carrier lifetime.

In seeking a basic understanding of these results, we have the challenge that, while the DFT band structure calculations for IrO_2 have generally been experimentally confirmed by ARPES measurements on IrO_2 films, within the accuracy of that technique, although there are discernible differences between the measurement and calculation for the anisotropically strained (110) films up to a film thickness of 16 nm,[10,17] we have measured the SHC to be ∼10 times the prediction and of opposite sign. (We comment that theoretical underestimation of the SHC is also an issue in simpler spin Hall materials such as Pt and Pt alloys.[32,33]) While keeping that disagreement in mind we note that the band structure calculations[15,16] and ARPES measurements show,[18] as mentioned above, that the IrO_2 rutile crystal structure possesses two types of DNLs. The DFT calculations predict that the SOC-induced anticrossing of bands forming type-1 DNLs near the Fermi energy can provide a large contribution to the SHC. We suggest that this DNL enhancement is sensitive to anisotropic strain because level splitting induced by interactions other than SOC should reduce the band mixing because of SOC near the DNLs and thereby reduce the spin Berry curvature. The strain may also shift the DNLs away from an optimum position relative to the Fermi level (see Supporting Information). The distinctly different values and behavior for σ_{SH}^{eff} between the (001) and (110) films, correlated with the absence and presence of anisotropic strain in the two cases, strongly support the role of DNLs in determining the amplitude of the SHC, notwithstanding the disagreement between theoretical prediction and experimental results with respect to both amplitude and sign. Along this line of argument, it also seems reasonable to attribute the smaller variation of the SHC between the current flow in [1$\bar{1}$0] and [001] directions of the (110) plane to the modulation of the SHC by the anisotropic strain in those films.

https://dx.doi.org/10.1021/acsami.0c16485
ACS Appl. Mater. Interfaces 2020, 12, 55411−55416

We further note the stark difference between $SrIrO_3$ and IrO_2, as the (001) IrO_2 film exhibits a three times stronger (six times after correcting spin attenuation though the Ir spacer) SHC than $SrIrO_3$, which requires octahedral rotation and strong electron correlation to maximize its SHC. It appears that strong electron correlation and a narrow conduction band, by itself, are not essential for obtaining a very high SHC.

4. CONCLUSIONS

We have measured a very strong, orientation-dependent SHE in epitaxial (001) and anisotropically strained (110) IrO_2 thin films with σ_{SH} 10 times higher and opposite in sign compared to theoretical predictions.[15,16] Even with the insertion of a 1 nm thick Ir passivation layer, which significantly attenuates the spin current, ξ_{DL} is 0.45 ± 0.03 at RT and 0.65 at 30 K for the higher resistivity, isotropically strained (001) films. Accounting for the spin attenuation of the 1 nm Ir spacer and assuming T_{int} of approximately 50%, the bulk value of σ_{SH} would be increased by a factor of four. For the (110) films, σ_{SH}^{eff} is lower, while still well above the predicted values for IrO_2, and is anisotropic between the current flow in the $[1\bar{1}0]$ and [001] directions. We tentatively attribute the lower ξ_{DL} (lower σ_{SH}^{eff}) of the anisotropically strained (110) films, compared to that of the (001) films, to level splittings that reduce the spin Berry curvature near the type-1 DNLs and associated strain-induced shifts in the DNL energies. These results support the theoretical conclusion that the DNLs play a significant role in the large SHE in IrO_2, despite the quantitative disagreement with the magnitude and sign of the experimental results. The (001) film results, combined with the ease of growth of IrO_2 epitaxial films, are very promising for application. Achieving a quantitatively correct understanding of the extraordinarily large SHE in a material with strong DNL but a broad t_{2g} conduction band appears to be a continuing theoretical challenge.

■ ASSOCIATED CONTENT

Supporting Information

The Supporting Information is available free of charge at https://pubs.acs.org/doi/10.1021/acsami.0c16485.

Additional details of the growth and characterization of IrO_2 thin films, sample preparation, and ST-FMR measurements and analysis (PDF)

■ AUTHOR INFORMATION

Corresponding Author

Arnab Bose − *School of Applied and Engineering Physics, Cornell University, Ithaca, New York 14853, United States;* orcid.org/0000-0003-4696-3112; Email: ab2729@cornell.edu

Authors

Jocienne N. Nelson − *Department of Physics, Cornell University, Ithaca, New York 14853, United States*

Xiyue S. Zhang − *School of Applied and Engineering Physics, Cornell University, Ithaca, New York 14853, United States*

Priyamvada Jadaun − *Department of Electrical and Computer Engineering, The University of Texas at Austin, Austin, Texas 78712, United States*

Rakshit Jain − *Department of Physics, Cornell University, Ithaca, New York 14853, United States*

Darrell. G. Schlom − *Department of Materials Science and Engineering, Cornell University, Ithaca, New York 14853, United States; Kavli Institute at Cornell for Nanoscale Science, Ithaca, New York 14853, United States;* orcid.org/0000-0003-2493-6113

Daniel. C. Ralph − *Department of Physics, Cornell University, Ithaca, New York 14853, United States; Kavli Institute at Cornell for Nanoscale Science, Ithaca, New York 14853, United States*

David. A. Muller − *School of Applied and Engineering Physics, Cornell University, Ithaca, New York 14853, United States; Kavli Institute at Cornell for Nanoscale Science, Ithaca, New York 14853, United States;* orcid.org/0000-0003-4129-0473

Kyle. M. Shen − *Department of Physics, Cornell University, Ithaca, New York 14853, United States; Kavli Institute at Cornell for Nanoscale Science, Ithaca, New York 14853, United States*

Robert. A. Buhrman − *School of Applied and Engineering Physics, Cornell University, Ithaca, New York 14853, United States*

Complete contact information is available at: https://pubs.acs.org/10.1021/acsami.0c16485

Author Contributions

A.B. and R.A.B. designed the experiment and wrote the first draft of the manuscript. A.B. did the sample fabrication, performed the spin torque experiments, and analyzed the data. J.N.N. grew the IrO_2 thin films and performed surface characterization with input from K.M.S and D.G.S. STEM images were obtained and analyzed by X.S.Z. with the input from D.A.M. R.J. assisted in the low-temperature measurements. D.C.R. provided comments and suggestions through the course of the work and helped in writing the final draft. P.J. performed DFT calculations of the band structure. All the authors contributed to discussing the results and the final version of the manuscript.

Funding

This work was supported in part by the National Science Foundation's MRSEC program (DMR-1719875) through the Cornell Center for Materials Research, the NSF's Platform for the Accelerated Realization, Analysis, and Discovery of Interface Materials (PARADIM) under Cooperative Agreement no. DMR-1539918, the Office of Naval Research (N00014-19-1-2143), and the NSF (DMR-1709255). R.J. was supported by the US Department of Energy (DE-SC0017671). Sample fabrication was performed at the Cornell Nanofabrication Facility/National Nanotechnology Coordinated Infrastructure, which is supported by the NSF (ECCS-1542081).

Notes

The authors declare no competing financial interest.

■ ACKNOWLEDGMENTS

We thank Ryan Tapping for providing data on the spin-torque efficiency of Ir films, and Celesta Chang and M. Thomas for assistance with the STEM/EELS studies. We are thankful to Jake Sun for preparing additional IrO_2 films. We also acknowledge the Texas Advanced Computing Center at The University of Texas at Austin (https://www.tacc.utexas.edu) for providing HPC resources that have contributed to the research results reported within this paper.

REFERENCES

(1) Sinova, J.; Valenzuela, S. O.; Wunderlich, J.; Back, C. H.; Jungwirth, T. Spin Hall Effects. *Rev. Mod. Phys.* **2015**, *87*, 1213−1260.

(2) Haney, P. M.; Lee, H.-W.; Lee, K.-J.; Manchon, A.; Stiles, M. D. Current Induced Torques and Interfacial Spin-Orbit Coupling: Semiclassical Modeling. *Phys. Rev. B: Condens. Matter Mater. Phys.* **2013**, *87*, 174411.

(3) Mellnik, A. R.; Lee, J. S.; Richardella, A.; Grab, J. L.; Mintun, P. J.; Fischer, M. H.; Vaezi, A.; Manchon, A.; Kim, E.-A.; Samarth, N.; Ralph, D. C. Spin-Transfer Torque Generated by a Topological Insulator. *Nature* **2014**, *511*, 449−451.

(4) Fan, Y.; Upadhyaya, P.; Kou, X.; Lang, M.; Takei, S.; Wang, Z.; Tang, J.; He, L.; Chang, L.-T.; Montazeri, M.; Yu, G.; Jiang, W.; Nie, T.; Schwartz, R. N.; Tserkovnyak, Y.; Wang, K. L. Magnetization Switching through Giant Spin-Orbit Torque in a Magnetically Doped Topological Insulator Heterostructure. *Nat. Mater.* **2014**, *13*, 699−704.

(5) MacNeill, D.; Stiehl, G. M.; Guimaraes, M. H. D.; Buhrman, R. A.; Park, J.; Ralph, D. C. Control of spin-orbit torques through crystal symmetry in WTe2/ferromagnet bilayers. *Nat. Phys.* **2017**, *13*, 300−305.

(6) Li, P.; Wu, W.; Wen, Y.; Zhang, C.; Zhang, J.; Zhang, S.; Yu, Z.; Yang, S. A.; Manchon, A.; Zhang, X.-x. Spin-Momentum Locking and Spin-Orbit Torques in Magnetic Nano-Heterojunctions Composed of Weyl Semimetal WTe2. *Nat. Commun.* **2018**, *9*, 3990.

(7) Armitage, N. P.; Mele, E. J.; Vishwanath, A. Weyl and Dirac Semimetals in Three-Dimensional Solids. *Rev. Mod. Phys.* **2018**, *90*, 15001.

(8) Nie, Y. F.; King, P. D. C.; Kim, C. H.; Uchida, M.; Wei, H. I.; Faeth, B. D.; Ruf, J. P.; Ruff, J. P. C.; Xie, L.; Pan, X.; Fennie, C. J.; Schlom, D. G.; Shen, K. M. Interplay of Spin-Orbit Interactions, Dimensionality, and Octahedral Rotations in Semimetallic SrIrO3. *Phys. Rev. Lett.* **2015**, *114*, 016401.

(9) Patri, A. S.; Hwang, K.; Lee, H.-W.; Kim, Y. B. Theory of Large Intrinsic Spin Hall Effect in Iridate Semimetals. *Sci. Rep.* **2018**, *8*, 8052.

(10) Kawasaki, J. K.; Uchida, M.; Paik, H.; Schlom, D. G.; Shen, K. M. Evolution of Electronic Correlations across the Rutile, Perovskite, and Ruddelsden-Popper Iridates with Octahedral Connectivity. *Phys. Rev. B* **2016**, *94*, No. 121104(R).

(11) Nan, T.; Anderson, T. J.; Gibbons, J.; Hwang, K.; Campbell, N.; Zhou, H.; Dong, Y. Q.; Kim, G. Y.; Shao, D. F.; Paudel, T. R.; Reynolds, N.; Wang, X. J.; Sun, N. X.; Tsymbal, E. Y.; Choi, S. Y.; Rzchowski, M. S.; Kim, Y. B.; Ralph, D. C.; Eom, C. B. Anisotropic Spin-Orbit Torque Generation in Epitaxial SrIrO3 by Symmetry Design. *Proc. Natl. Acad. Sci. U.S.A.* **2019**, *116*, 16186−16191.

(12) Wang, H.; Meng, K.-Y.; Zhang, P.; Hou, J. T.; Finley, J.; Han, J.; Yang, F.; Liu, L. Large Spin-Orbit Torque Observed in Epitaxial SrIrO3 Thin Films. *Appl. Phys. Lett.* **2019**, *114*, 232406.

(13) Liu, L.; Qin, Q.; Lin, W.; Li, C.; Xie, Q.; He, S.; Shu, X.; Zhou, C.; Lim, Z.; Yu, J.; Lu, W.; Li, M.; Yan, X.; Pennycook, S. J.; Chen, J. Current-Induced Magnetization Switching in All-Oxide Heterostructures. *Nat. Nanotechnol.* **2019**, *14*, 939−944.

(14) Everhardt, A. S.; Dc, M.; Huang, X.; Sayed, S.; Gosavi, T. A.; Tang, Y.; Lin, C.-C.; Manipatruni, S.; Young, I. A.; Datta, S.; Wang, J.-P.; Ramesh, R. Tunable Charge to Spin Conversion in Strontium Iridate Thin Films. *Phys. Rev. Mater.* **2019**, *3*, No. 051201(R).

(15) Sun, Y.; Zhang, Y.; Liu, C.-X.; Felser, C.; Yan, B. Dirac Nodal Lines and Induced Spin Hall Effect in Metallic Rutile Oxides. *Phys. Rev. B* **2017**, *95*, 235104.

(16) Jadaun, P.; Register, L. F.; Banerjee, S. K. Rational Design Principles for Giant Spin Hall Effect in 5d-Transition Metal Oxides. *Proc. Natl. Acad. Sci. U.S.A.* **2020**, *117*, 11878−11886.

(17) Fujiwara, K.; Fukuma, Y.; Matsuno, J.; Idzuchi, H.; Niimi, Y.; Otani, Y.; Takagi, H. 5d iridium oxide as a material for spin-current detection. *Nat. Commun.* **2013**, *4*, 2893.

(18) Nelson, J. N.; Ruf, J. P.; Lee, Y.; Zeledon, C.; Kawasaki, J. K.; Moser, S.; Jozwiak, C.; Rotenberg, E.; Bostwick, A.; Schlom, D. G.; Shen, K. M.; Moreschini, L. Dirac nodal lines protected against spin-orbit interaction in IrO2. *Phys. Rev. Mater.* **2019**, *3*, 64205.

(19) Xu, X.; Jiang, J.; Shi, W. J.; Süß, V.; Shekhar, C.; Sun, S. C.; Chen, Y. J.; Mo, S.-K.; Felser, C.; Yan, B. H.; Yang, H. F.; Liu, Z. K.; Sun, Y.; Yang, L. X.; Chen, Y. L. Strong Spin-Orbit Coupling and Dirac Nodal Lines in the Three-Dimensional Electronic Structure of Metallic Rutile IrO2. *Phys. Rev. B* **2019**, *99*, 195106.

(20) Barin, I. *Thermochemical Data of Pure Substances*; VCH, 1995.

(21) Diebold, U. The Surface Science of Titanium Dioxide. *Surf. Sci. Rep.* **2003**, *48*, 53−229.

(22) Supporting Information.

(23) Kawasaki, J. K.; Kim, C. H.; Nelson, J. N.; Crisp, S.; Zollner, C. J.; Biegenwald, E.; Heron, J. T.; Fennie, C. J.; Schlom, D. G.; Shen, K. M. Engineering Carrier Effective Masses in Ultrathin Quantum Wells of IrO2. *Phys. Rev. Lett.* **2018**, *121*, 176802.

(24) Kawasaki, J. K.; Baek, D.; Paik, H.; Nair, H. P.; Kourkoutis, L. F.; Schlom, D. G.; Shen, K. M. Rutile IrO2/TiO2 Superlattices: A Hyperconnected Analog to the Ruddelsden-Popper Structure. *Phys. Rev. Mater.* **2018**, *2*, 054206.

(25) Ryden, W. D.; Lawson, A. W.; Sartain, C. C. Electrical Transport Properties of IrO2 and RuO2. *Phys. Rev. B: Solid State* **1970**, *1*, 1494.

(26) Liu, L.; Moriyama, T.; Ralph, D. C.; Buhrman, R. A. Spin-Torque Ferromagnetic Resonance Induced by the Spin Hall Effect. *Phys. Rev. Lett.* **2011**, *106*, 036601.

(27) Pai, C.-F.; Ou, Y.; Vilela-Leão, L. H.; Ralph, D. C.; Buhrman, R. A. Dependence of the Efficiency of Spin Hall Torque on the Transparency of Pt/Ferromagnetic Layer Interfaces. *Phys. Rev. B: Condens. Matter Mater. Phys.* **2015**, *92*, 064426.

(28) Bose, A.; Dutta, S.; Bhuktare, S.; Singh, H.; Tulapurkar, A. A. Sensitive Measurement of Spin-Orbit Torque Driven Ferromagnetic Resonance Detected by Planar Hall Geometry. *Appl. Phys. Lett.* **2017**, *111*, 162405.

(29) Ramamoorthy, M.; Vanderbilt, D.; King-Smith, R. D. First-Principles Calculations of the Energetics of Stoichiometric TiO2 Surfaces. *Phys. Rev. B: Condens. Matter Mater. Phys.* **1994**, *49*, 16721−16727.

(30) Ishikuro, Y.; Kawaguchi, M.; Kato, N.; Lau, Y.-C.; Hayashi, M. Dzyaloshinskii-Moriya Interaction and Spin-Orbit Torque at the Ir/Co Interface. *Phys. Rev. B* **2019**, *99*, 134421.

(31) Tanaka, T.; Kontani, H.; Naito, M.; Naito, T.; Hirashima, D. S.; Yamada, K.; Inoue, J. Intrinsic Spin Hall Effect and Orbital Hall Effect in 4d and 5d Transition Metals. *Phys. Rev. B: Condens. Matter Mater. Phys.* **2008**, *77*, 165117.

(32) Zhu, L.; Zhu, L.; Sui, M.; Ralph, D. C.; Buhrman, R. A. Variation of the Giant Intrinsic Spin Hall Conductivity of Pt with Carrier Lifetime. *Sci. Adv.* **2019**, *5*, No. eaav8025.

(33) Zhu, L.; Buhrman, R. A. Maximizing Spin-Orbit-Torque Efficiency of Pt/Ti Multilayers: Trade-Off Between Intrinsic Spin Hall Conductivity and Carrier Lifetime. *Phys. Rev. Appl.* **2019**, *12*, 051002.

(34) Ou, Y.; Wang, Z.; Chang, C. S.; Nair, H. P.; Paik, H.; Reynolds, N.; Ralph, D. C.; Muller, D. A.; Schlom, D. G.; Buhrman, R. A. Exceptionally High, Strongly Temperature Dependent, Spin Hall Conductivity of SrRuO3. *Nano Lett.* **2019**, *19*, 3663−3670.

https://dx.doi.org/10.1021/acsami.0c16485
ACS Appl. Mater. Interfaces 2020, 12, 55411−55416